The Actin-Based Nanomachine at the Leading Edge of Migrating Cells

Vivek C. Abraham, Vijaykumar Krishnamurthi, D. Lansing Taylor, and Frederick Lanni
Center for Light Microscope Imaging and Biotechnology, and Department of Biological Sciences, Carnegie Mellon University, Pittsburgh, Pennsylvania 15213 USA

ABSTRACT Two fundamental parameters of the highly dynamic, ultrathin lamellipodia of migrating fibroblasts have been determined—its thickness in living cells (176 ± 14 nm), by standing-wave fluorescence microscopy, and its F-actin density (1580 ± 613 μm of F-actin/μm^3), via image-based photometry. In combination with data from previous studies, we have computed the density of growing actin filament ends at the lamellipodium margin (241 ± 100/μm) and the maximum force (1.86 ± 0.83 nN/μm) and pressure (10.5 ± 4.8 kPa) obtainable via actin assembly. We have used cell deformability measurements (Erickson, 1980. *J. Cell Sci.* 44:187–200; Petersen et al., 1982. *Proc. Natl. Acad. Sci. USA.* 79:5327–5331) and an estimate of the force required to stall the polymerization of a single filament (Hill, 1981. *Proc. Natl. Acad. Sci. USA.* 78:5613–5617; Peskin et al., 1993. *Biophys. J.* 65:316–324) to argue that actin assembly alone could drive lamellipodial extension directly.

INTRODUCTION

Locomoting fibroblasts typically extend remarkably thin, highly dynamic cytoplasmic domains called *lamellipodia* from their anterior margins. The protrusive activity of these domains allows the establishment of new contacts with the substratum. Although the force-producing mechanism associated with the protrusive activity of the lamellipodium is still a matter of debate, a dynamic actin cytoskeleton is thought to be required (Wehland et al., 1977; Wang, 1985; Forscher and Smith, 1988; Theriot and Mitchison, 1992; Fisher et al., 1988). Elucidation of the role of actin in lamellipodial protrusion will require quantification of its dynamics with high resolution.

So far it has not been possible to probe lamellipodial structure in three dimensions by light microscopy, because the lamellipodium is considerably thinner than the axial resolution of conventional light microscopes. Electron microscopy performed on fixed fibroblasts, however, has shown that the lamellipodium is 110–160 nm thick (Abercrombie et al., 1971) and that it contains a very high concentration of actin filaments that are largely oriented 1) parallel to the direction of protrusion and 2) with their barbed ends abutting the lamellipodium margin (Small, 1981).

Fluorescence microscopy has proved to be a valuable tool for the study of the mechanisms involved in cellular activity because it allows quantitative, molecularly specific studies of living cells (Giuliano and Taylor, 1995). In standing-wave fluorescence microscopy (SWFM), an interference-based optical system is used to set up an axially periodic illumination pattern in which the node spacing of the standing-wave (SW) field is typically in the range of 180–480 nm. By shifting the SW fringes through the specimen, axial discrimination better than 50 nm can be obtained (Lanni et al., 1993). SWFM is a direct-imaging method and therefore has a speed advantage over scanning. We report the application of 1) SWFM to measure lamellipodial thickness in living fibroblasts and 2) image-based photometry, using single actin filaments as standard fluorescent objects, to determine the concentration of F-actin in the lamellipodium. These measurements allow us to define the lamellipodial compartment and the three-dimensional structure and dynamics of actin in this compartment with very high resolution. We discuss our findings with regard to previously proposed models of lamellipodial protrusion, focusing particularly on the hypothesis that actin assembly at the leading edge drives protrusion directly.

MATERIALS AND METHODS

Standing-wave fluorescence microscopy

In SWFM (Bailey et al., 1993) light waves interfere in the specimen in a pattern of planar fringes normal to the axis of the microscope and excite fluorescence with axially periodic weighting. The period (Δs) of the fringes depends on the excitation wavelength, the specimen refractive index, and the angle that the two interfering beams make with respect to the microscope axis, $\Delta s = \lambda/(2n \cos \theta_b)$, where θ_b is the angle of each beam with respect to the microscope axis. This corresponds to the axial spatial frequency $K = 2\pi/\Delta s$. In this study, the beam angle was set to produce fringes with a period of 180 or 270 nm. The phase of one of the beams is shifted with high precision to move the fringes axially relative to the specimen (Fig. 1 *a*). This process selectively transfers information to sequential images that would otherwise be superposed in a conventional image. Any SWFM image is a linear combination of the conventional image (i_{DC}), and two images (i_{sin} and i_{cos}) representing axial sine and cosine weighting of the object (Krishnamurthi et al., 1996): $i_{sw}(\phi) = i_{DC} + (\cos \phi) i_{cos} - (\sin \phi) i_{sin}$. These component images can be recovered by simple algebraic operations on three images acquired at distinct fringe positions. In practice, we shift the fringes by 1/4 node spacing (+90°) for the second image, and again (to +180°) for the third image, and refer to these images as q, r, and s (Fig. 3, *a–c*). In this case $i_{DC} = (q + s)/2$, $i_{cos} = (q - s)/2$, and $i_{sin} = r - (q + s)/2$. When the thickness of the specimen is

Received for publication 16 March 1999 and in final form 25 May 1999.
Address reprint requests to Dr. Frederick Lanni, Department of Biological Sciences, Box 32, Carnegie Mellon University, 4400 Fifth Avenue, Pittsburgh, PA 15213. Tel.: 412-268-3460; Fax: 412-268-6571; E-mail: lanni@andrew.cmu.edu.

0006-3495/99/09/1721/12 $2.00

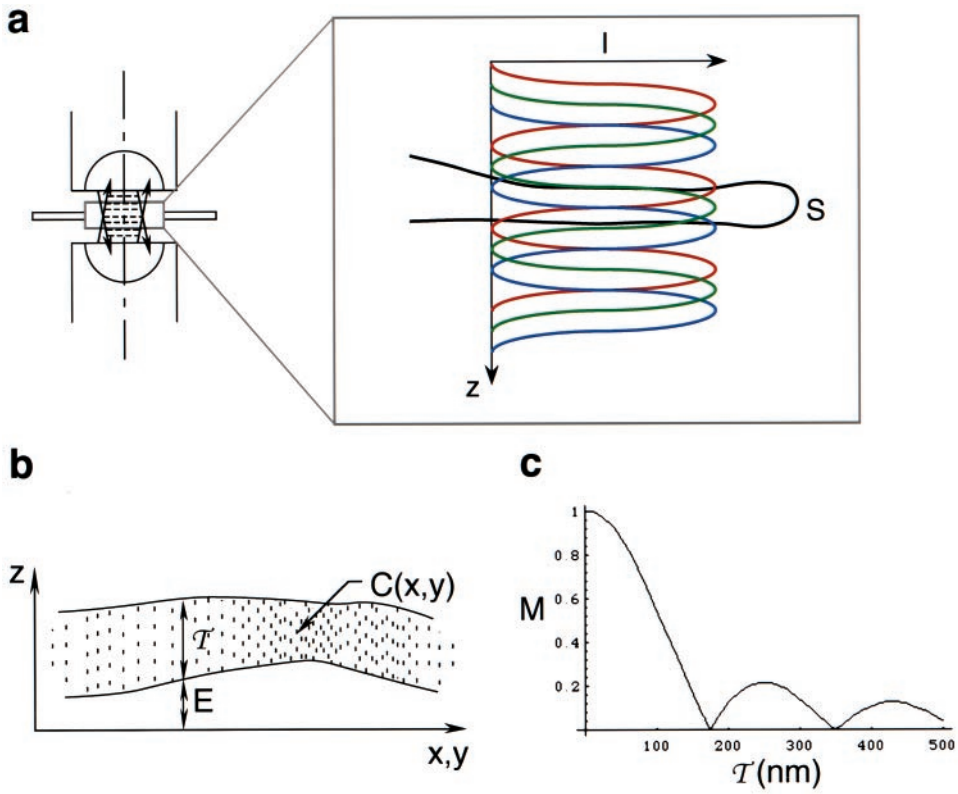

FIGURE 1 Imaging and thickness determination via SWFM. (*a*) Schematic diagram of SW microscope, showing two interfering beams of s-polarized coherent light, and the orientation of the resulting standing-wave field. Fluorescence excited by the field is imaged conventionally onto a cooled CCD camera. By shifting the phase of one of the two crossed beams, the fringes can be moved with high precision (along the *z* axis) relative to the specimen. Three distinct settings of the excitation field are shown in red, green, and blue. We express the fringe shift as a phase angle (ϕ), with the range 0–360° corresponding to an axial advance of one full cycle. When ϕ is shifted continuously, the measured fluorescence at any point in the image varies cyclically. The fluorescence modulation (M) can be computed for any pixel in which three distinct points on the curve $F(\phi)$ are known. I, Intensity; S, specimen. (*b*) Fluorescent stratum model, in which the specimen elevation (E), thickness ($\mathcal{T}$), and concentration of label (C) can vary with transverse coordinates. $C(x,y)$ is assumed to be homogeneous in the axial direction, so that $C\mathcal{T}$ is proportional to the total fluorescent label at location x,y. (*c*) Fluorescence modulation (M) as a function of stratum thickness, where the node spacing of the standing-wave field = 180 nm, $M = |\mathrm{sinc}(K\mathcal{T}/2)|$. M is ideally 100% for a fluorescent plane ($\mathcal{T} = 0$), decreasing monotonically to a null, where $\mathcal{T}$ equals the SW fringe spacing.

less than Δs, as in the case of lamellipodia, sharpness of focus carries no 3D information beyond the axial location of the object. In this case, we acquire one in-focus *q*-*r*-*s* image triplet. For thicker specimens, an image triplet is acquired at each plane of focus.

For measurements of thickness and fluorophore concentration via SWFM, the lamellipodium was modeled as an axially uniform fluorescent stratum (Fig. 1 *b*). In the model, elevation (E), thickness ($\mathcal{T}$), and concentration (C) are functions of image-plane coordinates, with $C\mathcal{T}$ giving the total signal in each pixel. Under computer control, the periodic excitation field is shifted through the specimen. This causes the fluorescence measured in any image pixel to cycle between a maximum and minimum value with a percentage modulation (M) and phase shift (ϕ_0) that depend upon local specimen thickness and elevation, respectively. In practice, a triplet of images is acquired with specific intervening shifts of the SW field. This is necessary and sufficient for computation of M, ϕ_0, and the DC image, which is equivalent to the conventional fluorescence image. The cyclic variation of the fluorescence with ϕ can be expressed in every pixel as $F(\phi) = (\text{const.})[1 + M\cos(\phi - \phi_o)]$. Experimentally, the modulation (M) is defined in each pixel by the maximum and minimum values of the brightness: $M = (F_{max} - F_{min})/(F_{max} + F_{min})$. In the fluorescent stratum model, this experimentally derived parameter is simply related to the stratum thickness ($\mathcal{T}$) by $M = |\mathrm{sinc}(K\mathcal{T}/2)|$, where K is the axial spatial frequency of the SW field, 23–35 radians/μm. Over most of its range, M is an invertible function from which $\mathcal{T}$ can be computed on a pixel-by-pixel basis as a thickness map of the object. The minimum and maximum values of F generally do not occur in the images *q*, *r*, and *s*. Therefore, we first generate a sequence of synthetic images, using $F'(\phi) = i_{DC} + (\cos\phi)i_{cos} - (\sin\phi)i_{sin}$. For each pixel, we find F_{max} and F_{min} in the sequence and compute M. Fig. 1 *c* shows that for $0.22 < M \leq 1$, we can determine $\mathcal{T}$ uniquely as $(2/K)\mathrm{arcsinc}(M)$. Images are acquired on a computer-controlled inverted microscope (Carl Zeiss, Thornwood, NY) modified for SWFM and equipped with a 14-bit cooled CCD camera (Photometrics, Tucson, AZ). Image triplets are corrected for nonsignal counts by subtraction of the image of a blank specimen, with any negative pixel values in the result set to zero. From the corrected images, we compute synthetic images (F') for 16 values of ϕ between 0 and 2π. F_{max} and F_{min} are found by sorting, M is computed, and $\mathcal{T}$ is found in a lookup table for all pixels in which i_{DC} is above a set threshold.

Fluorescent thin films

Polymethacryloyl chloride (25% in dioxane; Polysciences, Warrington, PA) was diluted to 5% in dioxane and reacted with aminotetramethylrhodamine and excess dry methanol to generate poly(methylmethacrylate) (PMMA) covalently labeled at 1 mol% (dye:PMMA residue). After a reaction period of 5 h (dark), the mixture was put on ice and neutralized with excess triethylamine. A red solid (rhod-PMMA) was recovered after solvent removal. To remove free dye, the polymer was washed in water, followed by methanol. After drying, it was determined by microscopy that

polymer particles were highly fluorescent and insoluble in UV-curing optical cement (NOA 61; Edmund Scientific Company, Barrington, NJ) used for mounting the film for SWFM. For making thin films, dry rhod-PMMA was made up as a solution in chlorobenzene.

Thin films for verification of SWFM were spin-cast on 40-mm round coverglasses (Fisher Scientific, Pittsburgh, PA), selected by use of a coherent green mercury lamp ($\lambda = 546.1$ nm; Edmund Scientific Company) to view reflection interference fringes. Selected coverglasses possessed a uniform long-range wedge showing parallel fringes, not necessarily uniformly spaced. One to eight drops of the polymer solution were applied to a coverglass spinning on a spin-caster at ~3000 rpm to produce a PMMA film over most of the glass surface. Cotton swabs wet with tetrahydrofuran were used to remove PMMA along two parallel boundaries, leaving a ≤1 cm band of film running normal to the fringes. Under the coherent lamp, fringes in the film area were shifted relative to those on bare glass (Fig. 2 *a*). By use of the coherent lamp and a 45° plate beam splitter, reflection interferograms of each coverglass were recorded at *f*/16 with a 35-mm camera located at a distance of 30.5 cm. The optics were aligned so that the center of each coverglass was at the point of normal incidence. Developed 35-mm film frames were scanned and digitized (SprintScan 35; Polaroid), and the fringe spacing and shift were determined with an image analysis software package (IPLab Spectrum). The relationship between the fractional fringe shift ($\Delta L/L$), the film refractive index ($n = 1.49$ for PMMA), the wavelength (λ), and the thickness ($\mathcal{T}$) simplifies to $\Delta L/L = 2n\mathcal{T}/\lambda$ at normal incidence. This relationship was used without further correction to compute $\mathcal{T}$ from measured values of $\Delta L/L$. Spectrophotometry of a 180-nm film gave a typical tetramethylrhodamine absorbance curve, with peak extinction (A_{556}) corresponding to an effective dye concentration of 7.8 mM in the film. The films showed no detectable birefringence between crossed polars. Coverglasses with films in the range of 20–220 nm were then mounted in optical cement, and the cement was polymerized by exposure to a low-power UV lamp.

Imaging of fixed lamellipodia via SWFM

Mouse Swiss 3T3 cells were grown to confluence under standard conditions on coverglasses (DeBiasio et al., 1988). An artificial wound was made in the monolayer by removal of all cells beyond a straight boundary. Cells along the wound edge spontaneously extend highly dynamic lamellipodia and migrate into the cleared region. At 1.5–3 h after the wound-healing response is initiated, the cells were simultaneously fixed and permeabilized at 37°C for 2–3 min in 0.5% glutaraldehyde and 0.15% saponin in cytoskeletal buffer (137 mM NaCl, 5 mM KCl, 1.1 mM Na_2HPO_4, 0.4 mM KH_2PO_4, 4 mM $NaHCO_3$, 2 mM $MgCl_2$, 5.5 mM glucose, 2 mM EGTA, 5 mM piperazine-*N*,*N*′-bis(2-ethanesulfonic acid), pH 6.0–6.1). This step was monitored by use of video-enhanced phase-contrast microscopy to 1) assess the quality of fixation and 2) determine lamellipodial activity at the instant of fixation. The mixture of glutaraldehyde and saponin in the fixation buffer was found to provide good preservation of dynamic lamellipodia. Extraction of F-actin is thought to be negligible when fixation and permeabilization are carried out simultaneously (Small et al., 1995). The cells were then transferred to 1% glutaraldehyde in cytoskeletal buffer for 9 min at 37°C. Standard methods for borohydride reduction and staining F-actin with rhodamine phalloidin (RhPh) were followed (Conrad et al., 1989), except that no further detergent extraction steps were performed. Specimens were mounted in gelvatol mounting medium (5.7 mM Tris, pH 7.4, 30% glycerol, 1% *n*-propyl gallate, 143 mg/ml polyvinyl alcohol; Air Products and Chemicals, Allentown, PA) with a refractive index of 1.38 and sealed in a coverglass sandwich, with two strips of food-wrap film as spacers. SW images were background subtracted, and a complete cycle of images was computed from the triplet image set to find the maximum and minimum fluorescence values for each pixel and the corresponding phase angle. For computation of thickness maps, the data were masked to include only regions having sufficient signal above background. For imaging of fixed lamellipodia, the SW node spacing, Δs, was set at 180 nm.

After image processing, the relative concentration of F-actin as a function of distance from the lamellipodial margin was determined by obtaining line intensity profiles drawn perpendicular to the leading edge in fluorophore concentration maps (Fig. 3 *f*). Each line profile was normalized to unity at the leading edge. The concentration at different points rearward was then expressed as a fraction of the concentration at the leading edge. Data from 17 lamellipodia were pooled, and the fluorophore concentration was plotted versus distance from the leading edge (data not shown). The

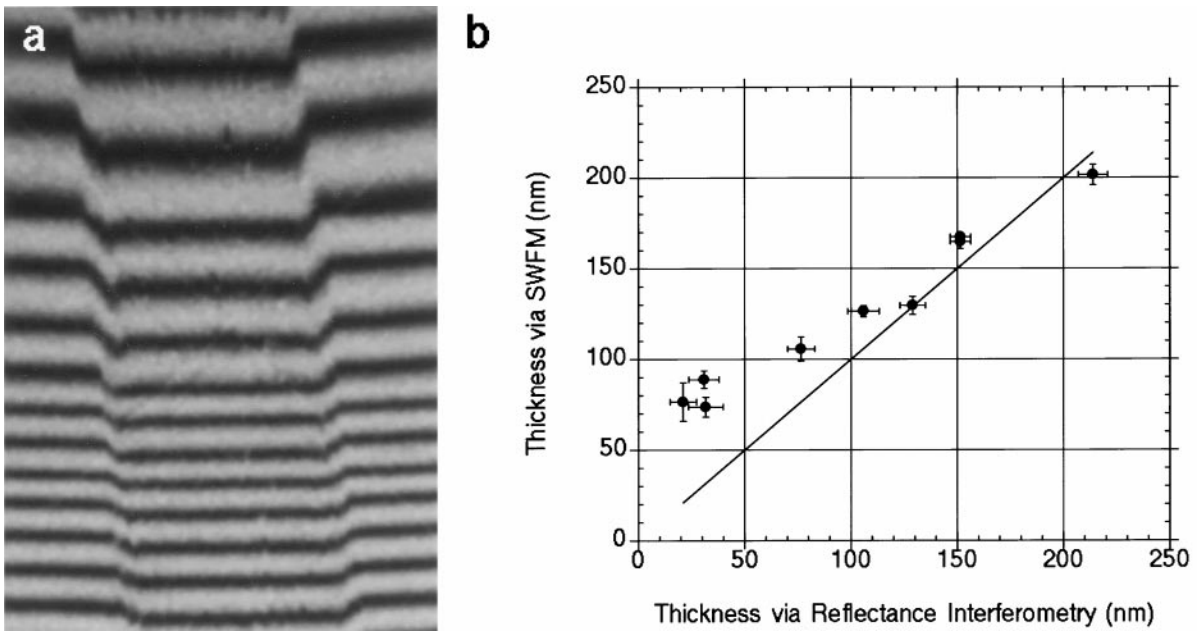

FIGURE 2 Thin fluorescent films as test objects for SWFM. (*a*) Reflection interferogram of PMMA film. The vertically oriented film strip is demarcated by the abrupt shift in the interference fringes. (*b*) Absolute PMMA film thickness derived from SWFM images versus that derived from reflectance interferometry. Error bars represent the standard deviation in estimates of film thickness for the same region of interest on the film. The line represents $y = x$.

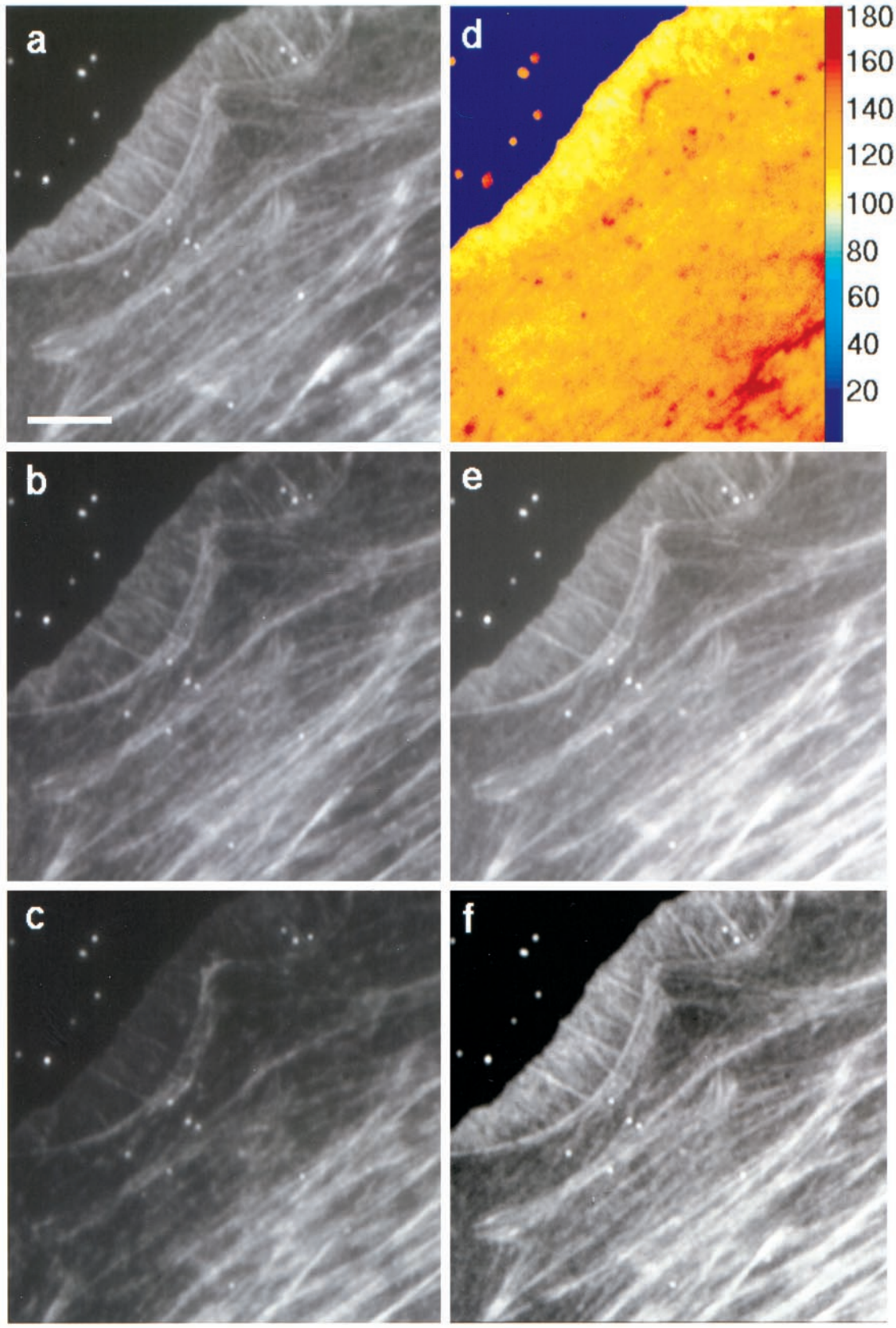

FIGURE 3 SWFM images of F-actin in a lamellipodium, and derived image maps. (*a–c*) SW image triplet, where the fringe shift was 1/4 of a full cycle (45 nm) between *a* and *b* and between *b* and *c*. (*d*) Thickness map, $\mathcal{T}(x,y)$. The color bar indicates the thickness in nm. (*e*) DC image, computed as the average of *a* and *c*. (*f*) Concentration map, $C(x,y)$, computed as the ratio image (*e*)÷(*d*). Bar = 5 μm.

distribution of data points was found to fit the line $y = 1.01 - 0.09x$ (correlation coefficient = 0.64).

Imaging of living cells via SWFM

Migrating 3T3 fibroblasts along a wound edge were microinjected with 5 mg/ml 10 kDa rhodamine-labeled dextran (Molecular Probes, Eugene, OR) dissolved in 2 mM piperazine-*N*,*N*′-bis(2-ethanesulfonic acid), pH 7.3. After allowing ~1 h for recovery under incubator conditions, the cells were mounted in complete culture medium under a 25-mm coverglass, using food-wrap film as a spacer. The specimen was sealed with melted VALAP (lanolin:vaseline:paraffin 1:1:1) and imaged immediately. The cells appeared to be healthy and motile in such a preparation for at least 1 h. On the microscope stage the temperature of the specimen was maintained at 37°C by circulating warm water through coils of copper tubing fit snugly around the dual oil-immersion objectives of the SW microscope. Temperature was monitored via a calibrated thermistor placed in the immersion oil of one objective. Control of specimen temperature was achieved by adjusting the flow rate and/or temperature of the circulating water. The major experimental constraint associated with imaging living cells is the time scale of lamellipodial dynamics. Trials established that at 37°C, SWFM image triplets captured within 1.5 s eliminated movement artefacts in most data sets. To achieve this speed, we installed a mask and operated the CCD camera in an expose/shift mode, reading out three rectangular images simultaneously in one full frame. Exposures of 200–400 ms gave sufficient speed and signal above background for reliable image processing. Photobleaching under these conditions was not significant. For imaging of living cells Δs was set at 270 nm.

Image-based photometry

Migrating 3T3 fibroblasts were fixed, and cellular F-actin was labeled with RhPh as described above. Rabbit skeletal muscle actin (Spudich and Watt, 1971) was polymerized in vitro, fixed by dilution in 1% glutaraldehyde in cytoskeletal buffer for 4–5 min, and incubated with RhPh. This solution of labeled filaments was used as mounting medium for the labeled cells. The specimen was sealed with VALAP and incubated at room temperature for ≥4 h to allow RhPh to equilibrate between its bound and free forms. We expect this incubation period to be adequate for equilibration, given the measured rate constants for the binding of rhodamine phalloidin to F-actin (De La Cruz and Pollard, 1994). Lamellipodia and substratum-bound filaments were imaged via conventional epifluorescence microscopy with a cooled CCD camera (Photometrics). A fixed excitation irradiance was used to image both lamellipodia and single filaments adsorbed to the substratum. The exposure time required to image single filaments with sufficient dynamic range was 23-fold greater than that used for lamellipodia. Lamellipodial brightness and on-axis filament brightness were determined by line intensity profiles. The brightness of lamellipodia and exogenous filaments was normalized with respect to exposure time, given the linear response of the cooled CCD camera. The measured fluorescence of single filaments above background was affected by fading that occurred during the long exposure (7 s) required to image them. The initial filament brightness, I_{fil}, was estimated by use of the relation $I_{fil} = f_1^2 \ln(f_1/f_2)/(f_1 - f_2)$, where f_1 and f_2 are on-axis filament brightness values from two consecutive exposures. The on-axis brightness of a filament was determined by obtaining a line profile across its image after processing in the same manner as for the images of single fluorescent beads (see below). We find that the degree of fading was not the same in different regions for a given specimen. This could be due to focus drift during the long exposure times used to image filaments and/or the error associated with manually focusing on different fields of filaments. The standard deviation in the corrected filament brightness for a given specimen was typically ~14% of the mean. The degree of fading of lamellipodial brightness was negligible, given the brief exposure to excitation (0.3 s).

Comparison of the brightness of single filaments and lamellipodia was made by treating the diffraction-limited image of a single filament as being due to a continuous string of point sources of fluorescence, the number of fluorophores per unit length (dn/dL) being constant. The lamellipodium was treated as a plane source of strength dn/dS dye molecules/μm^2. Integration of the point-spread function over plane and line sources, respectively, gives the average lamellipodium brightness (I_{lam}) in terms of dn/dS, and the on-axis filament brightness (I_{fil}) in terms of measured system optical parameters and dn/dL. To compensate for the effect of pixellation on the estimation of I_{fil}, single-filament images were inverse-filtered and restored by band-limited interpolation (Lanni and Baxter, 1992; Kontoyannis et al., 1996) (Fig. 5). We measured the point spread function (psf) of our fluorescence microscope by imaging 0.1-μm fluorescent latex beads (Molecular Probes). The images of 59 individual beads were background-subtracted and processed via band-limited interpolation. The resulting images of centered beads were summed, and the summed image was rotationally averaged. The resulting 2D psf was fit to a 2D radial Gaussian normalized to unit strength. This function was integrated over a line source of strength dn/dL to obtain the value of the constant of proportionality between dn/dL and I_{fil}. For our imaging system the proportionality constant was found to be 1.45. The filament density in the lamellipodium is given by $dL/dS = (dn/dS)/(dn/dL) = 1.45 \times I_{lam}/I_{fil}$, where dL/dS is expressed as μm of actin filament per μm^2.

The exogenous labeled filaments must adhere to the coverslip bearing fixed cells if a meaningful comparison of the fluorescence intensities of lamellipodia and single filaments is to be made. This requires that exogenous filaments and cells be labeled separately. However, the value of dL/dS did not change systematically with concentration of RhPh used to label cells or filaments (data not shown). This is expected for an equilibrated system consisting of free RhPh and RhPh bound to both cellular and exogenous actin. The substantial uncertainty in the value of dL/dS (see Results) reflects, in part, the variation in lamellipodial brightness observed for cells in a given specimen. However, the variation may also be due to 1) unknown error in focusing on single actin filaments and 2) variations observed between different fixed specimens that have been prepared on the same day and in the same manner. Controls performed with fixed cells whose F-actin had been saturated with unlabeled phalloidin revealed that the exogenously added fixed filaments have no significant affinity for fixed cells.

Analysis of electron micrographs

The acute angles subtended by distinct actin filament ends and the lamellipodium margin were measured using electron micrographs kindly provided by Dr. J. V. Small. The mean angle was determined from images of six lamellipodia ($n = 295$ filaments). The angle distribution for individual lamellipodia were not significantly different.

The density of assembling filament ends was estimated from electron micrographs (Small, 1981; Fig. 2, *a* and *b*), which were analyzed by drawing a line of known length parallel to and near the margin of lamellipodia. The number of distinct actin filaments that intersected a given scale micron on this line was considered to be the number of filaments (or filament ends) present per μm of margin.

RESULTS

Calibrated test objects for SWFM

A set of standard objects was developed for verification of SWFM instrument control and image-processing algorithms. To eliminate uncertainty in refractive structure and dye distribution inherent in using fluorescent microspheres embedded in optical cement, thin films of fluorescent PMMA were made by spin-casting. The thickness of such films was then measured by reflectance interferometry (Fig. 2 *a*). Specimens prepared from measured films were imaged by SWFM, and the thickness maps were computed from

%*M*. Good agreement between SWFM and interferometry was obtained in the thickness range spanning our biological specimens (Fig. 2 *b*). At this point we are unable to provide a good explanation for the disagreement between SWFM and reflectance interferometry for films thinner than 100 nm. We note only that this could be a result of the mounting step performed between reflectance interferometry and SWFM (see Materials and Methods).

TABLE 1 Thickness of fibroblast lamellipodia

Label	Group	Mean thickness ± SD (*n*), in nm
Rhodamine phalloidin (fixed F-actin)	All	113 ± 15 (19)
	Protruding	118 ± 10 (6)
	Stable	125 ± 15 (3)
Cytoplasmic volume marker (living cytoplasm)	All	176 ± 14 (11)

Application of SWFM to fibroblast lamellipodia

The stratum model was used first to analyze SWFM images of the fixed actin meshwork in fibroblast lamellipodia. Swiss 3T3 fibroblasts were stimulated to produce lamellipodia by "wounding" a confluent monolayer (DeBiasio et al., 1988), then fixing and labeling cellular F-actin with RhPh (Fig. 3). Processing of the image data acquired using SWFM allowed mapping of the thickness of the lamellipodial actin meshwork (Fig. 3 *d*). $\mathcal{T}$ was found to decrease anterogradely to uniform regions close to the leading edge. Within 2 μm of the edge, the actin meshwork thickness averaged 113 ± 15 nm (mean ± SD, $n = 19$). This implies an upper bound of 14 actin filaments that could be "stacked" in the meshwork at the leading edge of a living fibroblast. We are aware that the stratum model is only an approximation for a fixed lamellipodium in which the F-actin is fluorescently labeled. However, our result is consistent with electron microscope data that show fixed fibroblast lamellipodia to be 110–160 nm thick (Abercrombie et al., 1971). Our data also show that actin bundles within the lamellipodium are generally not significantly thicker than the fine meshwork that surrounds them. The DC image (Fig. 3 *e*) shows the frequently observed decrease in total fluorescence associated with F-actin rearward from the leading edge. This is thought to represent a decrease in the F-actin density, although the image shows total fluorescence and is not corrected for path length. The fluorescence concentration map (Fig. 3 *f*), which is the ratio image obtained by dividing the DC image by the thickness map for the same cell, shows that the concentration of F-actin does decrease retrogradely. The average lamellipodium showed a decrease of 9% of the F-actin density at the leading edge for every micron traversed in the rearward direction. Subsets of the lamellipodia imaged were classified as protruding or stable, based on their activity at the instant of fixation. This was recorded in time-lapse movies, using video-enhanced phase-contrast microscopy (data not shown). No significant difference was found in the thickness of these two classes (Table 1).

For measurements on living 3T3 cells, we also utilized the wound-healing monolayer preparation in which cells at the wound edge were microinjected with a cytoplasmic volume marker (Fig. 4). In this case, the application of the fluorescent stratum model is more realistic relative to the fixed cell case, because the fluorescent cytoplasmic marker is expected to be distributed uniformly along the axial dimension within the lamellipodium. Within 1 μm of the leading edge, the cytoplasmic compartment in living lamellipodia averaged 176 ± 14 nm ($n = 11$ lamellipodia), significantly thicker than the fixed actin meshwork. This is consistent with the effect of gel osmotic forces arising from Brownian motion of individual filaments in the living cell and axial shrinkage of the cytoskeletal meshwork upon fixation and subsequent processing. We believe that the actin meshwork occupies the entire cytoplasmic volume of the lamellipodium in a living cell because 1) actin-associated transport of beads is observed on both surfaces of the lamellipodium (Harris and Dunn, 1972) and 2) the thickness of the fixed actin meshwork in fibroblast lamellipodia (this study) is similar to the thickness of thin-sectioned lamellipodia viewed by electron microscopy (Abercrombie et al., 1971).

Image-based photometry

Actin filament density in lamellipodia was estimated by quantitative comparison of the fluorescence of fixed single

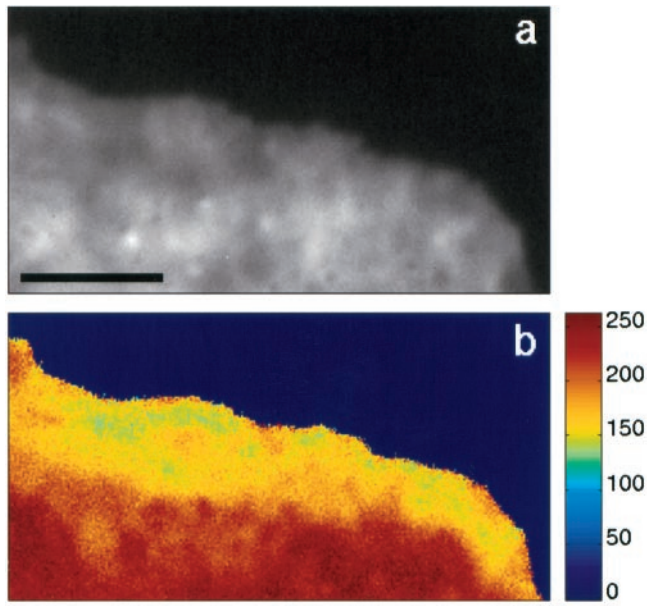

FIGURE 4 SWFM-derived image maps of lamellipodia in a living fibroblast. (*a*) Computed DC image. (*b*) Thickness map for the same cell. The color bar indicates the thickness in nm. The greater thickness of the lamellum (*red*) relative to the lamellipodium (*yellow/green*) is not obvious in *a* because the former contains organelles that probably exclude the microinjected rhodamine dextran. Bar = 5 μm.

actin filaments to that of fixed lamellipodia after labeling of both cellular and exogenous filaments with RhPh (Fig. 5). The specimens imaged contained both labeled cells and exogenously added labeled filaments that adhered to the substratum. The use of this approach, which we call image-based photometry, is contingent upon two conditions. First, the RhPh bound to cellular and exogenous F-actin is in equilibrium with unbound RhPh. Hence the computed actin filament density in the lamellipodium should be independent of the total quantity of RhPh present in the specimen. Our results suggest that this is true over a fivefold range in RhPh concentration (83–413 nM) (data not shown). Second, the affinity of cellular F-actin for RhPh is similar to that of the exogenous F-actin. We believe this to be generally true because in vitro binding and functional studies have shown that diverse F-actin binding proteins do not compete with RhPh for binding to F-actin, cofilin being a notable exception (De La Cruz and Pollard, 1994; Dancker et al., 1975; Nishida et al., 1987). Furthermore, cellular F-actin from leukocyte lysates and rabbit skeletal muscle actin have been reported to have similar affinities for RhPh (Cano et al., 1992). The filament density in the lamellipodium, dL/dS, is directly proportional to the ratio of the brightness of lamellipodia and that of single filaments. Lamellipodia were ~190-fold brighter than filaments, placing dL/dS at the leading edge at 278 ± 106 μm filament/μm^2. This result represents data collected from 10 specimens (64 lamellipodia). It can be argued that the filament density reported with this method could be substantially different from that observed in living cells, particularly because of shrinkage that typically accompanies fixation. However, any shrinkage that occurs must occur only along the axial dimension, because time-lapse movies show that the fixation and permeabilization steps do not induce any shrinkage of the lamellipodium along the plane parallel to the substratum. Therefore, we believe that it is reasonable to use the value of dL/dS reported here with the thickness of living lamellipodia to estimate the F-actin concentration in the lamellipodia of living cells (see Discussion and Table 2).

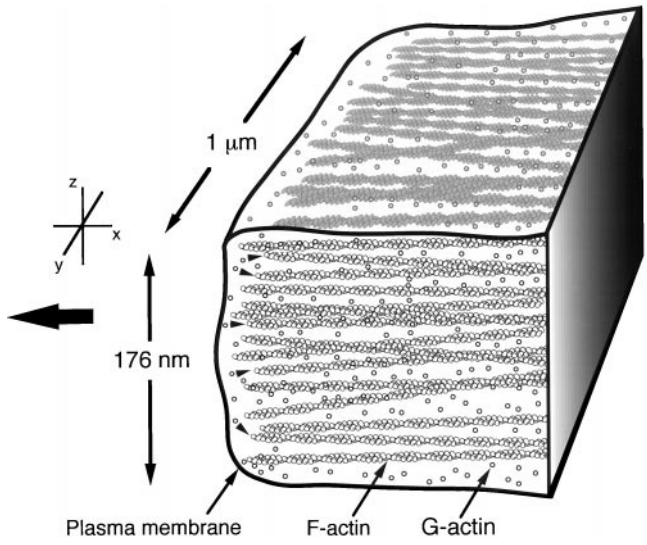

FIGURE 6 The actin nanomachine at the leading edge. The large arrow indicates the direction of protrusion. To accurately represent the experimentally determined actin content, the cytoplasmic volume shown would have to contain ~240 microfilaments and 180 unassembled monomers. This is a snapshot of a system in which the F-actin is moving rearward at the rate of 230 nm/s and 2.3×10^4 monomers assemble/s into filaments at the leading edge (Table 2). Arrowheads indicate monomer assembly onto barbed ends of preexisting filaments. The actin filament detail was taken from Alberts et al. (1994), figure 16–49 (B), with permission.

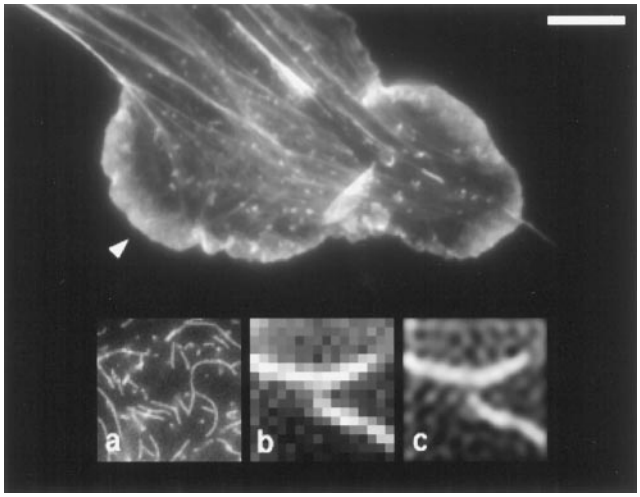

FIGURE 5 Estimation of F-actin density in the fibroblast lamellipodium. The arrowhead indicates the lamellipodium. *Insets*: (*a*) Raw image showing single RhPh-labeled F-actin at the same magnification as the image of the cell. Most spots and shorter segments represent filaments that only partly adhere to the substratum. (*b*) Magnified raw image of a sparse field of RhPh-labeled actin filaments. (*c*) Image of the same filaments after processing via band-limited interpolation. Bar = 10 μm.

DISCUSSION

Our data on lamellipodial thickness and F-actin density in fibroblasts can be combined with previous studies on actin dynamics to quantify several important features of actin assembly at the leading edge (Table 2). These include 1) the density of assembling filament ends at the lamellipodial margin, 2) the volume density of F-actin, 3) the minimum concentration gradient of unassembled actin at the margin required to support assembly, and 4) the maximum force and pressure that actin assembly could generate at the leading edge. The following sections discuss the important points with regard to the calculations summarized in Table 2.

The rate of actin assembly at the lamellipodial margin can be estimated directly from the rate of retrograde flow (V) observed in stationary, living lamellipodia by high-resolution differential interference contrast video microscopy (Fisher et al., 1988). In such lamellipodia V must fully account for the rate of actin assembly at the leading edge. We have assumed that actin assembly in such lamellipodia occurs under negligible load. The more direct measurement of the rate of retrograde flow made with a photoactivatable actin analog (Theriot and Mitchison, 1992) was not used,

TABLE 2 Actin assembly at the lamellipodial margin

Parameter	Mean (±SD)
Rate of rearward transport of actin meshwork in fibroblast lamellipodia (V)*	13.8 μm/min
Length increment per monomer for F-actin (l_0)#	2.72 nm/monomer
Mean acute angle subtended by actin filaments and lamellipodium margin (θ)	64.7 ± 16.5°
Rate of assembly of F-actin at the leading edge ($da/dt = V/l_0 \sin\theta$)	97 ± 16 monomers/filament/s
G-actin concentration ($\mathcal{G}$) at the leading edge ($da/dt = k_{on}\mathcal{G} - k_{off}$)§	8.5 ± 1.4 μM
Area density of F-actin at lamellipodial margin (dL/dS) (this study)	278 ± 106 μm of F-actin/μm^2
Thickness of living lamellipodium ($\mathcal{T}$) (this study)	176 ± 14 nm
F-actin density at lamellipodial margin $(dL/dS)/\mathcal{T}$	1580 ± 613 μm of F-actin/μm^3
Rate of F-actin assembly per μm of lamellipodial margin ($Q = V(dL/dS)$)	3840 ± 1460 μm/min
Rate of actin monomer assembly per μm of margin ($\mathcal{M} = Q/l_0$)	23,500 ± 8940 monomers/s
Number of barbed ends supporting actin assembly per μm of margin ($m = \mathcal{M}/(da/dt) = dL/dS \times \sin\theta$)	241 ± 100
Gradient in $\mathcal{G}$ at leading edge required to sustain actin assembly ($d\mathcal{G}/dx$)¶	≥7.28 ± 2.90 μM/μm
Density of barbed ends associated with front face of lamellipodium ($m/\mathcal{T}$)	1370 ± 578 /μm^2
Estimated stall force for the barbed end of a rigid, anchored actin filament (f)‖	7.7 ± 1.3 pN
∴ Stall force for a 10 μm-wide lamellipodium ($\mathcal{F} = 10 \times m \times f$)	18.6 ± 8.3 nN
∴ Stall pressure for a lamellipodium ($P = \mathcal{F}/10\mathcal{T}$)	10.5 ± 4.8 kPa

*Fisher et al. (1988).
#Egelman (1985).
§Pollard (1986).
¶Lanni and Ware (1984), Luby-Phelps et al. (1987).
‖Hill (1981); Peskin et al. (1993).

because those experiments were performed at 30–32°C. We have found lamellipodia to be extremely sensitive to temperature changes and to be far more dynamic at 37°C.

Of particular significance is our estimate of the volume density of F-actin at the leading edge, 1.58×10^3 μm filament/μm^3, which is equivalent to 40 mg/ml F-actin (Table 2). Our result for fibroblasts is significantly greater than the value of 10 mg/ml reported for the spread lamellae of macrophages (Hartwig and Shevlin, 1986). The combined effect of 1) nonspecific binding of RhPh and 2) autofluorescence of fixed specimens could result in an overestimation of actin density. Controls performed without RhPh show that autofluorescence, although substantial in the perinuclear region, is negligible at the cell periphery. The same is likely for nonspecifically bound RhPh, particularly because the fluorescence of RhPh is known to increase ninefold when it binds specifically to F-actin (Huang et al., 1992). The absolute F-actin density at the leading edge provides a calibration for the fluorophore concentration maps obtained via SWFM (Fig. 3 *f*). The ~45% retrograde decrease in F-actin concentration seen across a 5-μm lamellipod corresponds to the disassembly of 18 mg/ml filaments. Decreased cross-linking in the remaining meshwork at the rear of the lamellipodium may result in a greater gel osmotic pressure, thus explaining the greater thickness of this region (Figs. 3 *d* and 4 *b*). Second, we are able to estimate the number of free filament ends, 241 ± 100/μm of lamellipodial margin, a parameter that is only dependent on dL/dS and the angle subtended by individual filaments and the margin (Table 2). Our result is similar to an estimate of 110–130 filament ends/μm obtained via analysis of high-resolution electron micrographs of fibroblast lamellipodia (see Materials and Methods). However, the latter result must be an underestimate of the actual number of filament ends because of 1) the high F-actin density and 2) the likelihood that not all of the filament ends abut the margin (Chan et al., 1998).

The assembly process at the leading edge requires that there be a gradient in $\mathcal{G}$, the concentration of G-actin, to provide a forward flux of monomers (Olbris and Herzfeld, 1997). Unless mentioned otherwise, we use "G-actin" to refer to all unassembled, freely diffusible forms of actin (includes free monomers and actin complexed with monomer-sequestering proteins such as thymosin β and profilin). $\mathcal{M}$ and $\mathcal{T}$ were used to compute the monomer flux per unit area and the gradient in the concentration of unassembled actin, $d\mathcal{G}/dx$, that must exist at the lamellipodial margin. For our calculations we used 3.0×10^{-7} cm^2/s for the diffusion coefficient of G-actin ($D_{G\text{-actin}}$) in cytoplasm. This value is based on the diffusion coefficient of fluorescein-labeled actin in aqueous solution (Lanni and Ware, 1984) and the ratio of cytoplasmic and aqueous diffusion coefficients obtained for Ficoll particles that have a radius similar to that of an actin monomer (Luby-Phelps et al., 1987). The applicable value for $D_{G\text{-actin}}$ in cytoplasm is $\leq 3.0 \times 10^{-7}$ cm^2/s, given that 1) actin monomers are probably complexed with G-actin-binding proteins and 2) the unusually dense filamentous meshwork in the lamellipod may reduce $D_{G\text{-actin}}$ in the lamellipod further. Fick's law and the known monomer flux per unit area require that a gradient, $d\mathcal{G}/dx \geq 7.28 \pm 2.90$ μM/μm, exists across the lamellipod (Table 2). Across a 5-μm lamellipodium, $\mathcal{G}$ would therefore range steeply from 8 μM at the leading edge to 43 μM at the rear of the lamellipodium. We consider the latter value to be the cytoplasmic concentration of unassembled actin. To independently estimate the cytoplasmic concentration of unassembled actin, we used published values for 1) the total amount of actin/cell (7.1 pg), 2) the fraction of total protein

that is actin (3%), and 3) the fraction of actin that is filamentous (70%) (Heacock et al., 1984). The cytosolic concentration of total protein and, therefore, that of filamentous and nonfilamentous actin were calculated using the known refractive index of cytoplasm (Lanni et al., 1985) and refractive index increments of protein solutions (Barer, 1966). Using this approach, we estimate the concentration of unassembled actin in fibroblast-like cells to be 36 μM. Our experimental value for $d\mathcal{G}/dx$ does not take into account 1) disassembly of the meshwork that occurs as it moves rearward in the lamellipodium (Theriot and Mitchison, 1992) and 2) any additional forward flux of unassembled actin driven by solation-contraction in the rear of the locomoting cell (Post et al., 1995; DeBiasio et al., 1996). It should be pointed out that the concentration gradient for unassembled actin reported above assumes that the vast majority of unassembled actin that diffuses to the leading edge is freed to assemble onto filament ends at the leading edge. If this is not the case, the G-actin concentration at the leading edge would be >8 μM. However, the steepness of the gradient would remain unchanged, because it is only dependent on the net flux. Finally, because 8 μM is ~50-fold greater than the critical concentration for ATP-actin at the barbed end (Pollard, 1986), the unassembled actin that diffuses to the lamellipodial margin must be complexed with one or more monomer-sequestering proteins.

The quantitative definition of actin assembly at the lamellipodial margin allows evaluation of a model in which assembly directly generates protrusive force (reviewed in Condeelis, 1993; Cooper, 1991). The previous findings consistent with this model are that 1) actin assembly can generate sufficient force to deform lipid vesicles (Cortese et al., 1989), 2) cytochalasin B rapidly blocks protrusion when applied to growth cone lamellipodia (Forscher and Smith, 1988), 3) isolated brush border microvilli can extend via the assembly of exogenous monomeric actin (Mooseker et al., 1982), and 4) the Act-A protein from *L. monocytogenes*, when targeted at the plasma membrane of HeLa cells, causes substantial shape changes that appear to involve plasma membrane extension (Friederich et al., 1995). However, it has not been demonstrated that actin assembly at the leading edge can drive lamellipodial extension. Our results provide a way to estimate the pressure that could be generated via assembly and, therefore, a way to address this problem.

The protrusive force or pressure exerted by the protruding margin of fibroblast lamellipodia has not been measured directly. This is largely because this domain of the cell is extremely thin and highly dynamic. However, some insights can be gained from previously published studies of cell deformation. The negative pressure required to draw out a "protrusion" from the leading margin of adherent baby hamster kidney fibroblasts (Erickson, 1980) has been reported to be $\leq$0.2 kPa. In a separate study, the pressure required to indent the plasma membrane of the fibroblast lamellum by 1 μm was found to be within an order of magnitude of the former, ~1 kPa (Petersen et al., 1982). These results are consistent with 1) the notion that the pressure required to indent the plasma membrane and the underlying microfilamentous cortex is probably similar to that required to push it outward for small deformations and 2) the minimal hysteresis observed during cycles of deformation when the cell surface is indented at the physiological temperature of 37°C (Petersen et al., 1982). Both measurements of compliance described above involved deformation of the plasma membrane and the underlying cortex. The actin-based ultrastructure of the lamellipodium is well known to be markedly different from that of the cortex that envelopes the remainder of the cell; cortical F-actin consists of a mat of randomly oriented filaments, all approximately parallel to the plasma membrane, whereas lamellipodial filaments are oriented with their ends abutting the membrane. Consequently, the actin-based ultrastructure of the cortex must be remodeled before/during the initiation of protrusion to allow the concurrent assembly of the lamellipodial meshwork. In fact, gelsolin, an actin-severing, -capping, and -nucleating protein, has been shown to be a component of the Rac GTPase signaling pathway that regulates lamellipodial extension (Azuma et al., 1998), and a direct correlation exists between gelsolin expression levels and the rate of cell migration (Cunningham et al., 1991; Witke et al., 1995). Therefore, we infer that lamellipodial extension requires the deformation of the plasma membrane and only a fraction of the underlying cortex. Thus the measurements of cortical compliance can be considered to be upper limits on the pressure that must be applied to the plasma membrane to cause lamellipodial protrusion. In other words, the fact that the compliance measurements were made on a region of the cell surface that should offer significantly more resistance to deformation than the plasma membrane at the front face of a lamellipodium allows us to treat the reported range of deformation pressures as the range of pressures that would be more than sufficient to effect lamellipodial protrusion. As the measured cortical deformation pressures fall well below our estimate of 10.5 ± 4.8 kPa that could be generated via actin assembly at the lamellipodial margin (Table 2), it appears that assembly alone could drive protrusion. This would be true even if only 20% of the assembling filament ends contributed to force generation. Atomic force microscopy has also been used recently to measure Young's modulus at the leading edge (Rotsch et al., 1999). The reported upper limit for this parameter (5 kPa) leads us to conclude that our estimate of the pressure required to stall actin assembly at the margin is at least an order of magnitude greater than that required to generate a lamellipodium-like protrusion of length 5 μm at the leading edge. We arrived at this conclusion by treating the front face of the lamellipodium as a deformable plate, simply supported on all edges, on which a uniformly distributed pressure generated by actin assembly is applied (Baumeister et al., 1978). We note that our measurement of F-actin density at the leading edge could be lower than the actual density, given that proteins such as cofilin are known to compete with RhPh for binding to F-actin (Nishida et al.,

1987). However, any correction for such a systematic error would only increase our estimate of the pressure required to stall actin assembly at the leading edge, thus not affecting our conclusion. The thermodynamic model used to estimate the stall force, f, has been described previously (Hill, 1981; Peskin et al., 1993). The maximum protrusive force at the leading edge would be generated upon anchoring of the assembling actin meshwork relative to the substratum, so that the free energy of actin assembly may be fully coupled to protrusion. Therefore, we consider as a model a representative rigid, anchored, actin filament at the lamellipodium margin that supports monomer addition under a load. For such a system in the stalled state,

$$f = (kT/l_0 \sin\theta)\ln(\mathcal{G}k_{on}/k_{off})$$

where k is Boltzmann's constant, T is absolute temperature, $\mathcal{G}$ is the equivalent concentration of free G-actin, and k_{on} and k_{off} are the on and off rate constants, respectively, for ATP-actin at the barbed end (Pollard, 1986). We have made two assumptions in estimating the actin assembly force, which is expected to be at maximum in the stalled condition. First, the on and off rate constants for filament assembly at the lamellipodial margin are not affected by the presence of the plasma membrane, i.e., the assembling barbed ends spend a very small fraction of time in contact with the membrane. The physical basis for this assumption is that there are two main sources of fluctuations that lead to separation of the filament ends and the plasma membrane—the Brownian undulations of the plasma membrane and the Brownian deflection of the assembling filaments themselves, which are otherwise supported by the lamellipodial meshwork (Mogilner and Oster, 1996). Second, the unsupported length of a typical filament at the leading edge is short enough because of entanglement and cross-linking such that it will not bend significantly in the stalled condition. Any bending that occurs as the lamellipodium approaches the stalled state would only result in an increased stall force (Mogilner and Oster, 1996).

A complete model of lamellipodial extension has to take into account the rearward transport of the actin meshwork in the lamellipodium (Smith, 1988). Clearly, actin assembly at the margin could be coupled to both protrusion and rearward transport. The lamellipodium of a keratocyte has been shown to exert measurable traction forces (K. Burton and D. L. Taylor, unpublished results), which could arise from actin assembly at the margin and/or the action of anchored myosin motors. One or more myosins are probably involved in the force generation required for rearward transport since inhibition of myosin decreases the transport rate. Accompanying this decrease is a stimulation of protrusion at the leading edge, which could occur as a result of better engagement of the actin assembly engine with its load (Lin et al., 1996). Consistent with this scenario are 1) the extension of lamellipodia upon local disruption of myosin 1-β function in growth cones (Wang et al., 1996) and 2) the apparent role of myosin I family members in the maintenance of the cortical stiffness that inhibits ectopic lamellipodial protrusion in *D. discoideum* (Mermall et al., 1998). Our arguments do not consider the conditions required for rearward flow. Estimation of the stall force only requires that the actin meshwork in the lamellipodium be immobilized relative to the substratum.

Although we argue that actin assembly alone can generate ample force for lamellipodial protrusion, we cannot rule out the existence of other protrusive mechanisms. However, most models of protrusion propose a necessary role for F-actin. One such model, which has also been proposed for filopodial extension (Wang et al., 1996), suggests that an acto-myosin interaction at the leading edge generates the protrusive force (Condeelis, 1993). Second, protrusion may also be driven by the gel osmotic potential of the lamellipodial actin meshwork (Smith, 1988). This model is testable because it predicts that lamellipodia will thicken, possibly via the inactivation of F-actin cross-linking proteins, during the protrusive phase. Although our data from fixed lamellipodia indicate that no increase in thickness occurs during protrusion, the measurement must be performed on living cells to rule out fixation artefacts. Finally, the myosin II-driven solation-contraction in the rear of a locomoting cell probably assists the protrusive machinery by enhancing the delivery of disassembled cytoskeletal components to the leading edge and/or providing a positive hydrostatic pressure that aids in cell protrusion (Stossel, 1994; Post et al., 1995; DeBiasio et al., 1996). The latter is thought to play some role, especially when cell extensions assume the form of blebs (Cunningham, 1995). Our quantitative definition of actin dynamics at the leading edge, in combination with the future measurement of relevant, molecularly specific parameters in cells, is expected to aid our understanding of the protrusive machinery that operates during cell locomotion.

We thank B. Bailey for providing training and advice for SWFM, C. Bartosh for maintaining the supply of Swiss 3T3 fibroblasts, J. Hugdahl for synthesizing rhod-PMMA used to produce fluorescent films for SWFM, and D. Pane for implementing the frame-shift algorithm for fast imaging of living cells via SWFM. J. V. Small kindly provided electron micrographs for analysis. We also thank D. Velegol, G. S. Vanni, K. Burton, Y-L. Wang, P. Forscher, and J. Theriot for helpful discussions.

This work was supported by National Institutes of Health grant AR32461 to DLT, National Science Foundation grant MCB8920118 to DLT and FL, and a grant from Carl Zeiss, Inc.

REFERENCES

Abercrombie, M., J. E. Heaysman, and S. M. Pegrum. 1971. The locomotion of fibroblasts in culture. IV. Electron microscopy of the leading lamella. *Exp. Cell Res.* 67:359–367.

Alberts, B., D. Bray, J. Lewis, M. Raff, K. Roberts, and J. D. Watson. 1994. Molecular Biology of the Cell. Garland Publishing, New York.

Azuma, T., W. Witke, T. P. Stossel, J. H. Hartwig, and D. J. Kwiatkowski. 1998. Gelsolin is a downstream effector of rac for fibroblast motility. *EMBO J.* 17:1362–1370.

Bailey, B., D. L. Farkas, D. L. Taylor, and F. Lanni. 1993. Enhancement of axial resolution in fluorescence microscopy by standing-wave excitation. *Nature.* 366:44–48.

Barer, R. 1966. Phase contrast and interference microscopy in cytology. *In* Physical Techniques in Biological Research, Vol. III. A. W. Pollister, editor. Academic Press, New York. 16–17.

Baumeister, T., E. A. Avallone and T. Baumeister, III. 1978. Marks' Standard Handbook for Mechanical Engineers. McGraw-Hill, New York. 5-52–5-53.

Cano, M. L., L. Cassimeris, M. Joyce, and S. H. Zigmond. 1992. Characterization of tetramethylrhodaminyl-phalloidin binding to cellular F-actin. *Cell Motil. Cytoskeleton.* 21:147–158.

Chan, A. Y., S. Raft, M. Bailly, J. B. Wyckoff, J. E. Segall, and J. S. Condeelis. 1998. EGF stimulates an increase in actin nucleation and filament number at the leading edge of the lamellipod in mammary adenocarcinoma cells. *J. Cell Sci.* 111:199–211.

Condeelis, J. 1993. Life at the leading edge: the formation of cell protrusions. *Annu. Rev. Cell Biol.* 9:411–444.

Conrad, P. A., M. A. Nederlof, I. M. Herman, and D. L. Taylor. 1989. Correlated distribution of actin, myosin, and microtubules at the leading edge of migrating Swiss 3T3 fibroblasts. *Cell Motil. Cytoskeleton.* 14:527–543.

Cooper, J. A. 1991. The role of actin polymerization in cell motility. *Annu. Rev. Physiol.* 53:585–605.

Cortese, J. D., B. Schwab, III, C. Frieden, and E. L. Elson. 1989. Actin polymerization induces a shape change in actin-containing vesicles. *Proc. Natl. Acad. Sci. USA.* 86:5773–5777.

Cunningham, C. C. 1995. Actin polymerization and intracellular solvent flow in cell surface blebbing. *J. Cell Biol.* 129:1589–1599.

Cunningham, C. C., T. P. Stossel, and D. J. Kwiatkowski. 1991. Enhanced motility in NIH 3T3 fibroblasts that overexpress gelsolin. *Science.* 251:1233–1236.

Dancker, P., I. Low, W. Hasselbach, and T. Wieland. 1975. Interaction of actin with phalloidin: polymerization and stabilization of F-actin. *Biochim. Biophys. Acta.* 400:407–414.

DeBiasio, R. L., G. M. LaRocca, P. L. Post, and D. L. Taylor. 1996. Myosin II transport, organization, and phosphorylation: evidence for cortical flow/solation-contraction coupling during cytokinesis and cell locomotion. *Mol. Biol. Cell.* 7:1259–1282.

DeBiasio, R. L., L-L. Wang, G. W. Fisher, and D. L. Taylor. 1988. The dynamic distribution of fluorescent analogues of actin and myosin in protrusions at the leading edge of migrating Swiss 3T3 fibroblasts. *J. Cell Biol.* 107:2631–2645.

De La Cruz, E. M., and T. D. Pollard. 1994. Transient kinetic analysis of rhodamine phalloidin binding to actin filaments. *Biochemistry.* 33: 14387–14392.

Egelman, E. H. 1985. The structure of F-actin. *J. Muscle Res. Cell Motil.* 6:129–151.

Erickson, C. A. 1980. The deformability of BHK cells and polyoma virus-transformed BHK cells in relation to locomotory behavior. *J. Cell Sci.* 44:187–200.

Fisher, G. W., P. A. Conrad, R. L. DeBiasio, and D. L. Taylor. 1988. Centripetal transport of cytoplasm, actin, and the cell surface in lamellipodia of fibroblasts. *Cell Motil. Cytoskeleton.* 11:235–247.

Forscher, P., and S. J. Smith. 1988. Actions of cytochalasins on the organization of actin filaments and microtubules in a neuronal growth cone. *J. Cell Biol.* 107:1505–1516.

Friederich, E., E. Gouin, R. Hellio, C. Kocks, P. Cossart, and D. Louvard. 1995. Targeting of Listeria monocytogenes ActA protein to the plasma membrane as a tool to dissect both actin-based cell morphogenesis and ActA function. *EMBO J.* 14:2731–2744.

Giuliano, K. A., and D. L. Taylor. 1995. Measurement and manipulation of cytoskeletal dynamics in living cells. *Curr. Opin. Cell Biol.* 7:4–12.

Harris, A., and G. Dunn. 1972. Centripetal transport of attached particles on both surfaces of moving fibroblasts. *Exp. Cell Res.* 73:519–523.

Hartwig, J. H., and P. J. Shevlin. 1986. The architecture of actin filaments and the ultrastructural location of actin-binding protein in the periphery of lung macrophages. *J. Cell Biol.* 103:1007–1020.

Heacock, C. S., K. E. Eidsvoog, and J. R. Bamburg. 1984. The influence of contact-inhibited growth and of agents which alter cell morphology on the levels of G- and F-actin in cultured cells. *Exp. Cell Res.* 153: 402–412.

Hill, T. L. 1981. Microfilament or microtubule assembly or disassembly against a force. *Proc. Natl. Acad. Sci. USA.* 78:5613–5617.

Huang, Z. J., R. P. Haugland, W. M. You, and R. P. Haugland. 1992. Phallotoxin and actin binding assay by fluorescence enhancement. *Anal. Biochem.* 200:199–204.

Kontoyannis, N. S., B. Bailey, and F. Lanni. 1996. Measured and computed point spread functions for an indirect water immersion objective used in three-dimensional fluorescence. *Proc. Soc. Photo-optical Instrum. Eng.* 2655:34–42.

Krishnamurthi, V., B. Bailey, and F. Lanni. 1996. Image processing in 3-D standing-wave fluorescence microscopy. *Proc. Soc. Photo-optical Instrum. Eng.* 2655:18–25.

Lanni, F., B. Bailey, D. L. Farkas, and D. L. Taylor. 1993. Excitation field synthesis as a means for obtaining enhanced axial resolution in fluorescence microscopes. *Bioimaging.* 1:187–196.

Lanni, F., and G. Baxter. 1992. Sampling theorem for square-pixel image data. *Proc. Soc. Photo-optical Instrum. Eng.* 1660:140–147.

Lanni, F., A. S. Waggoner, and D. L. Taylor. 1985. Structural organization of interphase 3T3 fibroblasts studied by total internal reflection fluorescence microscopy. *J. Cell Biol.* 100:1091–1102.

Lanni, F., and B. R. Ware. 1984. Detection and characterization of actin monomers, oligomers, and filaments in solution by measurement of fluorescence photobleaching recovery. *Biophys. J.* 46:97–110.

Lin, C. H., E. M. Espreafico, M. S. Mooseker, and P. Forscher. 1996. Myosin drives retrograde F-actin flow in neuronal growth cones. *Neuron.* 16:769–782.

Luby-Phelps, K., P. E. Castle, D. L. Taylor, and F. Lanni. 1987. Hindered diffusion of inert tracer particles in the cytoplasm of mouse 3T3 cells. *Proc. Natl. Acad. Sci. USA.* 84:4910–4913.

Mermall, V., P. Post, and M. Mooseker. 1998. Unconventional myosins in cell movement, membrane traffic, and signal transduction. *Science.* 279:527–533.

Mogilner, A., and G. Oster. 1996. Cell motility driven by actin polymerization. *Biophys. J.* 71:3030–3045.

Mooseker, M. S., T. D. Pollard, and K. A. Wharton. 1982. Nucleated polymerization of actin from the membrane-associated ends of microvillar filaments in the intestinal brush border. *J. Cell Biol.* 95:223–233.

Nishida, E., K. Iida, N. Yonezawa, S. Koyasu, I. Yahara, and H. Sakai. 1987. Cofilin is a component of intranuclear and cytoplasmic actin rods induced in cultured cells. *Proc. Natl. Acad. Sci. USA.* 84:5262–5266.

Olbris, D. J., and J. Herzfeld. 1997. Variation of the rate of extension of actin networks. *In* Statistical Mechanics in Physics and Biology, Vol. 463. D. Wirtz and T. C. Halsey, editors. Materials Research Society, Pittsburgh, PA.

Peskin, C. S., G. M. Odell, and G. F. Oster. 1993. Cellular motions and thermal fluctuations: the Brownian ratchet. *Biophys. J.* 65:316–324.

Petersen, N. O., W. B. McConnaughey, and E. Elson. 1982. Dependence of locally measured cellular deformability on position on the cell, temperature, and cytochalasin B. *Proc. Natl. Acad. Sci. USA.* 79:5327–5331.

Pollard, T. D. 1986. Rate constants for the reactions of ATP- and ADP-actin with the ends of actin filaments. *J. Cell Biol.* 103:2747–2754.

Post, P. L., R. L. DeBiasio, and D. L. Taylor. 1995. A fluorescent protein biosensor of myosin ii regulatory light chain phosphorylation reports a gradient of phosphorylated myosin II in migrating cells. *Mol. Biol. Cell.* 6:1755–1768.

Rotsch, C., K. Jacobson, and M. Radmacher. 1999. Dimensional and mechanical dynamics of active and stable edges in motile fibroblasts investigated by using atomic force microscopy. *Proc. Natl. Acad. Sci. USA.* 96:921–926.

Small, J. V. 1981. Organization of actin in the leading edge of cultured cells: influence of osmium tetroxide and dehydration on the ultrastructure of actin meshworks. *J. Cell Biol.* 91:695–705.

Small, J. V., M. Herzog, and K. Anderson. 1995. Actin filament organization in the fish keratocyte lamellipodium. *J. Cell Biol.* 129:1275–1286.

Smith, S. J. 1988. Neuronal cytomechanics: the actin-based motility of growth cones. *Science.* 242:708–715.

Spudich, J. A., and S. Watt. 1971. The regulation of rabbit skeletal muscle contraction. I. Biochemical studies of the interaction of the tropomyosin-

troponin complex with actin and the proteolytic fragments of myosin. *J. Biol. Chem.* 246:4866–4871.

Stossel, T. P. 1994. The machinery of cell crawling. *Sci. Am.* 271:54–63.

Theriot, J. A., and T. J. Mitchison. 1992. Comparison of actin and cell surface dynamics in motile fibroblasts. *J. Cell Biol.* 118:367–377.

Wang, F. S., J. S. Wolenski, R. E. Cheney, M. S. Mooseker, and D. G. Jay. 1996. Function of myosin-V in filopodial extension of neuronal growth cones. *Science.* 273:660–663.

Wang, Y-L. 1985. Exchange of actin subunits at the leading edge of living fibroblasts: possible role of treadmilling. *J. Cell Biol.* 101:597–602.

Wehland, J., M. Osborn, and K. Weber. 1977. Phalloidin-induced actin polymerization in the cytoplasm of cultured cells interferes with cell locomotion and growth. *Proc. Natl. Acad. Sci. USA.* 74:5613–5617.

Witke, W., A. H. Sharpe, J. H. Hartwig, T. Azuma, T. P. Stossel, and D. J. Kwiatkowski. 1995. Hemostatic, inflammatory, and fibroblast responses are blunted in mice lacking gelsolin. *Cell.* 81:41–51.